



# Low-loss demonstration and refined characterization of silicon arrayed waveguide gratings in the near-infrared

ERIC J. STANTON,\* NICOLAS VOLET, AND JOHN E. BOWERS

Department of Electrical and Computer Engineering, University of California, Santa Barbara (UCSB), CA 93106, USA

\*estanton@ece.ucsb.edu

**Abstract:** A resonator is characterized with two cascaded arrayed waveguide gratings (AWGs) in a ring formation. From this structure, the on-chip transmittance of a single AWG is extracted, independent of coupling efficiency. It provides improved measurement accuracy, which is essential for developing AWGs with extremely low loss. Previous methods normalize the off-chip AWG transmittance to that of a reference waveguide with identical coupling, leading to an uncertainty of ~14 % on the extracted on-chip AWG transmittance. It is shown here that the proposed “AWG-ring” method reduces this value to ~3 %. A low-loss silicon AWG and an AWG-ring are fabricated. Channel losses with <2 dB are found, with a crosstalk per channel approaching -30 dB. Such an efficient wavelength multiplexing device is beneficial for the integration of spectroscopic sensors, multi-spectral lasers, and further progress in optical communication systems.

© 2017 Optical Society of America under the terms of the [OSA Open Access Publishing Agreement](#)

**OCIS codes:** (060.4230) Multiplexing; (140.3298) Laser beam combining; (130.3120) Integrated optics devices; (230.5750) Resonators.

## References and links

1. M. K. Smit, “New focusing and dispersive planar component based on an optical phased array,” *Electron. Lett.* **24**, 385–386 (1988).
2. H. Takahashi, S. Suzuki, K. Kato, and I. Nishi, “Arrayed-waveguide grating for wavelength division multi/demultiplexer with nanometre resolution,” *Electron. Lett.* **26**, 87–88 (1990).
3. C. Dragone, “An  $N \times N$  Optical Multiplexer Using a Planar Arrangement of Two Star Couplers,” *IEEE Photon. Technol. Lett.* **3**, 812–815 (1991).
4. K. Okamoto, K. Takiguchi, and Y. Ohmori, “16-channel optical add/drop multiplexer using silica-based arrayed-waveguide gratings,” *Electron. Lett.* **31**, 723–724 (1995).
5. M. J. O’Mahony, D. Simeonidou, D. K. Hunter, and A. Tzanakaki, “The application of optical packet switching in future communication networks,” *IEEE Commun. Mag.* **39**, 128–135 (2001).
6. P. Cheben, J. Schmid, A. Delâge, A. Densmore, S. Janz, B. Lamontagne, J. Lapointe, E. Post, P. Waldron, and D.-X. Xu, “A high-resolution silicon-on-insulator arrayed waveguide grating microspectrometer with sub-micrometer aperture waveguides,” *Opt. Express* **15**, 2299–2306 (2007).
7. B. G. Lee, J. Kinsky, A. K. Goyal, C. Pflügl, L. Diehl, M. A. Belkin, A. Sanchez, and F. A. Capasso, “Beam combining of quantum cascade laser arrays,” *Opt. Express* **17**, 16216–16224 (2009).
8. Z. Hu, A. Glidle, C. N. Ironside, M. Sorel, M. J. Strain, J. Cooper, and H. Yin, “Integrated microspectrometer for fluorescence based analysis in a microfluidic format,” *Lab Chip* **12**, 2850–2857 (2012).
9. B. I. Akca, B. Považay, A. Alex, K. Wörhoff, R. M. de Ridder, W. Drexler, and M. Pollnau, “Miniature spectrometer and beam splitter for an optical coherence tomography on a silicon chip,” *Opt. Express* **21**, 16648–16656 (2013).
10. A. Z. Subramanian, E. Ryckeboer, A. Dhakal, F. Peyskens, A. Malik, B. Kuyken, H. Zhao, S. Pathak, A. Ruocco, A. De Groote, P. Wuytens, D. Martens, F. Leo, W. Xie, U. D. Dave, M. Muneeb, P. Van Dorpe, J. Van Campenhout, W. Bogaerts, P. Bienstman, N. Le Thomas, D. Van Thourhout, Z. Hens, G. Roelkens, and R. Baets, “Silicon and silicon nitride photonic circuits for spectroscopic sensing on-a-chip,” *Photon. Res.* **3**, B47–B59 (2015).
11. A. Stoll, Z. Zhang, R. Haynes, and M. Roth, “High-Resolution Arrayed-Waveguide-Gratings in Astronomy: Design and Fabrication Challenges,” *Photonics* **4**, 30 (2017).
12. G. Carpintero, E. Rouvalis, K. Ławniczuk, M. Fice, C. C. Renaud, X. J. Leijtens, E. A. Bente, M. Chitoui, F. Van Dijk, and A. J. Seeds, “95 GHz millimeter wave signal generation using an arrayed waveguide grating dual wavelength semiconductor laser,” *Opt. Lett.* **37**, 3657–3659 (2012).

13. E. J. Stanton, M. J. R. Heck, J. Bovington, A. Spott, and J. E. Bowers, "Multi-octave spectral beam combiner on ultra-broadband photonic integrated circuit platform," *Opt. Express* **23**, 11272–11283 (2015).
14. H. Takahashi, S. Suzuki, and I. Nishi, "Wavelength multiplexer based on SiO<sub>2</sub>-Ta<sub>2</sub>O<sub>5</sub> arrayed-waveguide grating," *J. Lightw. Technol.* **12**, 989–995 (1994).
15. M. K. Smit and C. van Dam, "PHASAR-based WDM-devices: Principles, design and applications," *IEEE J. Sel. Topics Quantum Electron.* **2**, 236–250 (1996).
16. A. Sugita, A. Kaneko, K. Okamoto, M. Itoh, A. Himeno, and Y. Ohmori, "Very low insertion loss arrayed-waveguide grating with vertically tapered waveguides," *IEEE Photon. Technol. Lett.* **12**, 1180–1182 (2000).
17. K. Sasaki, F. Ohno, A. Motegi, and T. Baba, "Arrayed waveguide grating of 70 × 60 μm<sup>2</sup> size based on Si photonic wire waveguides," *Electron. Lett.* **41**, 801–802 (2005).
18. K. Okamoto, "Progress and technical challenge for planar waveguide devices: silica and silicon waveguides," *Laser Photon. Rev.* **6**, 14–23 (2012).
19. S. Pathak, M. Vanslembrouck, P. Dumon, D. Van Thourhout, P. Verheyen, G. Lepage, P. Absil, and W. Bogaerts, "Effect of Mask Discretization on Performance of Silicon Arrayed Waveguide Gratings," *IEEE Photon. Technol. Lett.* **26**, 718–721 (2014).
20. J. F. Bauters, J. R. Adleman, M. J. R. Heck, and J. E. Bowers, "Design and characterization of arrayed waveguide gratings using ultra-low loss Si<sub>3</sub>N<sub>4</sub> waveguides," *Appl. Phys. A* **116**, 427–432 (2014).
21. E. J. Stanton, A. Spott, M. L. Davenport, N. Volet, and J. E. Bowers, "Low-loss arrayed waveguide grating at 760 nm," *Opt. Lett.* **41**, 1785–1788 (2016).
22. M. Kohtoku, H. Sanjoh, S. Oku, Y. Kadota, Y. Yoshikuni, and Y. Shibata, "InP-based 64-channel arrayed waveguide grating with 50 GHz channel spacing and up to -20 dB crosstalk," *Electron. Lett.* **33**, 1786–1787 (1997).
23. B. I. Akca, C. R. Doerr, G. Sengo, K. Wörhoff, M. Pollnau, and R. M. de Ridder, "Broad-spectral-range synchronized flat-top arrayed-waveguide grating applied in a 225-channel cascaded spectrometer," *Opt. Express* **20**, 18313–18318 (2012).
24. T. Y. Fan, "Laser beam combining for high-power, high-radiance sources," *IEEE J. Sel. Topics Quantum Electron.* **11**, 567–577 (2005).
25. G. Kurczveil, M. J. Heck, J. D. Peters, J. M. Garcia, D. Spencer, and J. E. Bowers, "An integrated hybrid silicon multiwavelength AWG laser," *IEEE J. Sel. Topics Quantum Electron.* **17**, 1521–1527 (2011).
26. P. Trinh, S. Yegnanarayanan, F. Coppinger, and B. Jalali, "Silicon-on-insulator (SOI) phased-array wavelength multi/demultiplexer with extremely low-polarization sensitivity," *IEEE Photon. Technol. Lett.* **9**, 940–942 (1997).
27. M. J. R. Heck, J. F. Bauters, M. L. Davenport, J. K. Doylend, S. Jain, G. Kurczveil, S. Srinivasan, Y. Tang, and J. E. Bowers, "Hybrid Silicon Photonic Integrated Circuit Technology," *IEEE J. Sel. Topics Quantum Electron.* **19**, 6100117 (2013).
28. P. Dong, Y.-K. Chen, G.-H. Duan, and D. T. Neilson, "Silicon photonic devices and integrated circuits," *Nanophotonics* **3**, 215–228 (2014).
29. A. W. Fang, H. Park, O. Cohen, R. Jones, M. J. Paniccia, and J. E. Bowers, "Electrically pumped hybrid AlGaInAs-silicon evanescent laser," *Opt. Express* **14**, 9203–9210 (2006).
30. D. Liang and J. E. Bowers, "Recent progress in lasers on silicon," *Nat. Photon.* **4**, 511–517 (2010).
31. G. Roelkens, A. Abassi, P. Cardile, U. Dave, A. de Groote, Y. De Koninck, S. Dhoore, X. Fu, A. Gassenq, N. Hattasan, Q. Huang, S. Kumari, S. Keyvaninia, B. Kuyken, L. Li, P. Mechet, M. Muneeb, D. Sanchez, H. Shao, T. Spuesens, A. Z. Subramanian, S. Uvin, M. Tassaert, K. van Gasse, J. Verbist, R. Wang, Z. Wang, J. Zhang, J. van Campenhout, X. Yin, J. Bauwelinck, G. Morthier, R. Baets, and D. van Thourhout, "III-V-on-Silicon Photonic Devices for Optical Communication and Sensing," **2**, 969–1004 (2015).
32. T. Baehr-Jones, T. Pinguet, P. L. Guo-Qiang, S. Danziger, D. Prather, and M. Hochberg, "Myths and rumours of silicon photonics," *Nat. Photon.* **6**, 206–208 (2012).
33. P. Pottier, M. J. Strain, and M. Packirisamy, "Integrated microspectrometer with elliptical Bragg mirror enhanced diffraction grating on silicon on insulator," *ACS Photonics* **1**, 430–436 (2014).
34. A. Y. Piggott, J. Lu, K. G. Lagoudakis, J. Petykiewicz, T. M. Babinec, and J. Vučković, "Inverse design and demonstration of a compact and broadband on-chip wavelength demultiplexer," *Nat. Photon.* **9**, 374–377 (2015).
35. J. H. den Besten, M. P. Dessens, C. G. P. Herben, X. J. M. Leijtens, F. H. Groen, M. R. Leys, and M. K. Smit, "Low-loss, compact, and polarization independent PHASAR demultiplexer fabricated by using a double-etch process," *IEEE Photon. Technol. Lett.* **14**, 62–64 (2002).
36. C. R. Doerr, L. Zhang, and P. J. Winzer, "Monolithic InP multiwavelength coherent receiver using a chirped arrayed waveguide grating," *J. Lightw. Technol.* **29**, 536–541 (2011).
37. S. Janz, D.-X. Xu, J.-M. Baribeau, A. Delage, and R. L. Williams, "Si/Si<sub>1-x</sub>Ge<sub>x</sub> waveguide components for WDM demultiplexing," *Proc. SPIE* **3630**, 106–114 (1999).
38. A. Malik, M. Muneeb, S. Pathak, Y. Shimura, J. Van Campenhout, R. Loo, and G. Roelkens, "Germanium-on-silicon mid-infrared arrayed waveguide grating multiplexers," *IEEE Photon. Technol. Lett.* **25**, 1805–1808 (2013).
39. P. Barritault, M. Brun, P. Labeye, J.-M. Hartmann, F. Boulila, M. Carras, and S. Nicoletti, "Design, fabrication and characterization of an AWG at 4.5 μm," *Opt. Express* **23**, 26168–26181 (2015).
40. W. Bogaerts, S. K. Selvaraja, P. Dumon, J. Brouckaert, K. De Vos, D. Van Thourhout, and R. Baets, "Silicon-on-Insulator Spectral Filters Fabricated With CMOS Technology," *IEEE J. Sel. Topics Quantum Electron.* **16**, 33–44 (2010).

41. M. Muneeb, X. Chen, P. Verheyen, G. Lepage, S. Pathak, E. Ryckeboer, A. Malik, B. Kuyken, M. Nedeljkovic, J. Van Campenhout, G. Z. Mashanovich, and G. Roelkens, "Demonstration of Silicon-on-insulator mid-infrared spectrometers operating at 3.8  $\mu\text{m}$ ," *Opt. Express* **21**, 11659–11669 (2013).
42. J. Wang, Z. Sheng, L. Li, A. Pang, A. Wu, W. Li, X. Wang, S. Zou, M. Qi, and F. Gan, "Low-loss and low-crosstalk 8×8 silicon nanowire AWG routers fabricated with CMOS technology," *Opt. Express* **22**, 9395–9403 (2014).
43. G. Tittelbach, B. Richter, and W. Karthe, "Comparison of three transmission methods for integrated optical waveguide propagation loss measurement," *Pure Appl. Opt.* **2**, 683–706 (1993).
44. R. Adar, Y. Shani, C. H. Henry, R. C. Kistler, G. E. Blonder, and N. A. Olsson, "Measurement of very low-loss silica on silicon waveguides with a ring resonator," *Appl. Phys. Lett.* **58**, 444–445 (1991).
45. D. J. W. Klunder, F. S. Tan, T. van der Veen, H. F. Bulthuis, G. Sengo, B. Docter, H. J. W. M. Hoekstra, and A. Driessen, "Experimental and numerical study of SiON microresonators with air and polymer cladding," *J. Lightw. Technol.* **21**, 1099–1110 (2003).
46. A. Yariv, "Universal relations for coupling of optical power between microresonators and dielectric waveguides," *Electron. Lett.* **36**, 321–322 (2000).
47. Z. Shi and R. W. Boyd, "Fundamental limits to slow-light arrayed-waveguide-grating spectrometers," *Opt. Express* **21**, 7793–7798 (2013).
48. M. A. Tran, T. Komljenovic, J. C. Hulme, M. L. Davenport, and J. E. Bowers, "A Robust Method for Characterization of Optical Waveguides and Couplers," *IEEE Photon. Technol. Lett.* **28**, 1517–1520 (2016).
49. W. Eickhoff and R. Ulrich, "Optical frequency domain reflectometry in single-mode fiber," *Appl. Phys. Lett.* **39**, 693–695 (1981).
50. W. Hürlimann, *Encyclopedia of Statistical Sciences (Vol. 2)* (John Wiley & Sons, Inc., 2006), pp. 1031–1035, 2nd ed.
51. G. Li, J. Yao, H. Thacker, A. Mekis, X. Zheng, I. Shubin, Y. Luo, J.-H. Lee, K. Raj, J. E. Cunningham, and A. V. Krishnamoorthy, "Ultralow-loss, high-density SOI optical waveguide routing for macrochip interconnects," *Opt. Express* **20**, 12035–12039 (2012).
52. W. A. Zortman, D. C. Trotter, and M. R. Watts, "Silicon photonics manufacturing," *Opt. Express* **18**, 23598–23607 (2010).

## 1. Introduction

Arrayed waveguide gratings (AWGs) combine or split closely-spaced spectral channels of light [1–4]. They are ubiquitous in optical communication systems where wavelength division multiplexing (WDM) is used to expand network capacity [5]. As fundamental building blocks for spectroscopic sensors [6–11] and multi-spectral high-brightness light sources [12, 13], AWGs have prompted decades of research to optimize the device insertion loss, inter-channel crosstalk, and footprint, among other characteristics [1–3, 14–21]. Since the insertion loss of an AWG scales with its number of channels, devices with ultra-low loss (<2 dB loss per channel) are necessary when combining many wavelengths (*e.g.*, >5 for <10 dB cumulative loss) [22, 23]. Power scaling by spectral beam combining [24] or intra-cavity AWG lasers [12, 25] are some examples that require this level of performance. These AWG lasers have not recently been pursued due to the loss-penalty from an AWG within the laser cavity. However, further development to decrease AWG loss would enable this technology. In particular, silicon (Si) AWGs [26] with low loss and low crosstalk are desirable to design photonic integrated circuits (PICs) with WDM capability [18, 27, 28]. Such fully-integrated transceivers have been realized with the heterogeneous integration of lasers on Si [29–31]. AWGs along with other Si-based PIC components stand to benefit from large-volume infrastructures, currently used for complementary metal–oxide–semiconductor (CMOS) fabrication [32]. Besides AWGs, other WDM devices have been demonstrated with reduced footprint [33, 34]. However, they exhibit much higher loss and support fewer channels.

High-performance AWGs having loss <2 dB are prevalent with waveguide cores made of silicon dioxide (SiO<sub>2</sub>) [11, 16] or silicon nitride (Si<sub>3</sub>N<sub>4</sub>) [20, 21]. In contrast, the insertion loss reported in AWGs fabricated with tantalum pentoxide [14], indium phosphide [35, 36], germanium [37–39], or Si [19, 40–42] is still prohibitively large for high-power multi-spectral lasers. In all these reports, the AWG loss was extracted by normalizing its off-chip transmittance to that of a reference waveguide with similar facet geometry and, in some cases, similar propagation length and bends. Variation in coupling efficiency coarsely limits the accuracy of this method [43], in particular for low-loss devices [44, 45].

The Si AWG demonstrated in this work with loss <2 dB is characterized by a new method using a ring resonator. As schematized in Fig. 1(a), it contains two cascaded AWGs. This "AWG-ring" allows to drastically improve AWG characterization and rigorously define the crosstalk. The accuracy of this method is determined using data for the coupling uncertainty along with the modeled transmission spectrum of the AWG-ring. Both the waveguide method and the AWG-ring method are then compared with a statistical analysis of low-loss Si AWGs. Channel loss in the range of 1.2–1.6 dB are demonstrated, along with a crosstalk per channel near  $-29.1$  dB. These results substantiate the accuracy of the proposed characterization method and suggest that these Si AWGs have performance comparable to state-of-the-art devices based on  $\text{SiO}_2$  or  $\text{Si}_3\text{N}_4$ .

## 2. Model and simulations

A top-view schematic of the AWG free propagation region (FPR) is shown in Fig. 1(b). The AWG model developed in [20, 21] is extended here to account for the length  $L_{io}$  of the input and output waveguides and both FPRs. The electric field transfer function of an AWG is then expressed as:

$$\mathcal{A} = \sqrt{t_g} \exp(ik_0 n_{io} L_{io}) \sum_{j=1}^{N_{AW}} E_j (1 + \delta_j) \exp(i\theta_j), \quad (1)$$

with:

$$\theta_j \equiv k_0 [n_{AW} L_{AW,j} + n_{FPR} (r + L_{FPR,j})] + \phi_j, \quad (2)$$

where  $N_{AW}$  is the number of arrayed waveguides (AWs),  $t_g$  the transmittance from the waveguide grating to each de-multiplexed waveguide,  $k_0$  the free-space propagation constant, and  $r$  the Rowland radius [15]. The (complex) effective refractive indices  $n_{io}$ ,  $n_{AW}$ , and  $n_{FPR}$  correspond respectively to the input and output waveguides, the AWs, and the FPR. Parameters  $E_j$ ,  $\delta_j$  and  $\phi_j$  denote respectively the electric field amplitude at the input FPR interface, the amplitude error, and the phase error in AW  $j$  [20]. This AW has a length  $L_{AW,j}$  and  $L_{FPR,j}$  is the distance in the FPR from AW  $j$  to each de-multiplexed waveguide.

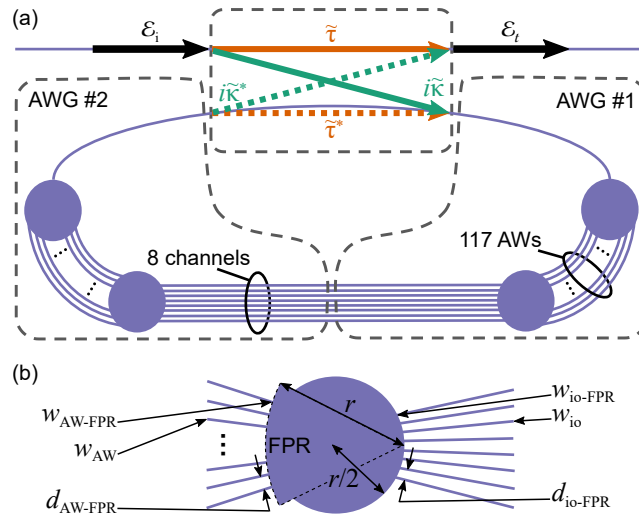


Fig. 1. (a) Diagram of the AWG-ring with complex amplitudes  $\mathcal{E}_i$  and  $\mathcal{E}_t$  of the input and output guided electric fields. Coupling between the bus and ring waveguides is characterized by  $\tilde{\tau}$  and  $\tilde{\kappa}$ . (b) Schematic of the AWG design parameters.

Concerning the AWG-ring, coupling from the bus to the resonator can be described by the complex coefficients  $\tilde{\kappa} = \kappa \exp(i\phi_{\tilde{\kappa}})$  and  $\tilde{\tau} = \tau \exp(i\phi_{\tilde{\tau}})$  defined in Fig. 1(a). Assuming this

coupling to be lossless, the following must hold [46]:  $\tau^2 + \kappa^2 = 1$ . Also, assuming both AWGs have the same transfer function  $\mathcal{A} = \sqrt{t_a} \exp(i\phi_{\mathcal{A}})$ , the on-chip AWG-ring transmittance  $t_r = |\mathcal{E}_t/\mathcal{E}_i|^2$  can be expressed as:

$$t_r = \left| \frac{\tilde{\tau} - \mathcal{A}^2}{1 - \tilde{\tau}^* \mathcal{A}^2} \right|^2 = \frac{\tau^2 + t_a^2 - 2\tau t_a \cos(\Phi)}{1 + (\tau t_a)^2 - 2\tau t_a \cos(\Phi)}, \quad (3)$$

where  $\Phi \equiv 2\phi_{\mathcal{A}} - \phi_{\tilde{\tau}}$  and  $t_a$  is the on-chip transmittance of an AWG.

An AWG and an AWG-ring with Si-core and SiO<sub>2</sub>-cladding waveguides are modeled with (1), (2), and (3). The AWG design follows the methodology detailed in [21] and the physical parameters are listed in Table 1. Notice that the relatively large footprint area  $S$  results from the low-loss design. This can be reduced, *e.g.*, by designing the AWGs with a higher modal group index at the expense of increased loss [47]. The calculated AWG transmittance  $t_a$  is plotted in the left axis of Fig. 2, whereas the right axis shows the transmittance  $t_r$  of the AWG-ring for  $\tau^2 = 0.15$ .

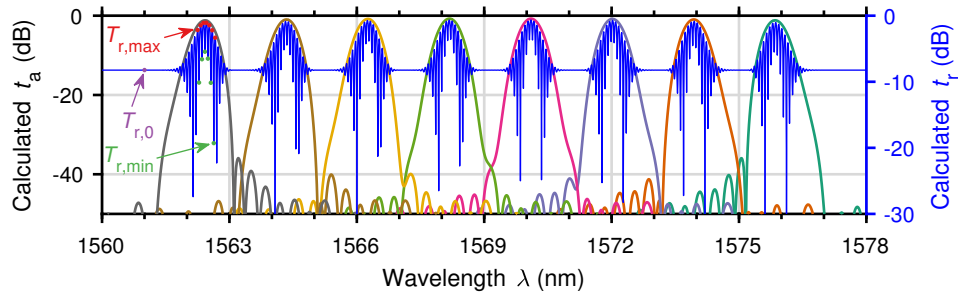


Fig. 2. On-chip transmission spectra calculated (left axis) for each channel of an AWG and (right axis) for an AWG-ring. Colored dots show examples of the three parameters defined in (5), for the ideal case where  $\eta = 1$ .

The off-chip transmittances  $T_a$  and  $T_r$  of the AWG and of the AWG-ring, respectively, include the input and output coupling efficiency, which is defined as:

$$\eta \equiv T_r/t_r = T_a/t_a. \quad (4)$$

This quantity depends on polishing quality (for facet coupling), lithography, etch uniformity, layer thicknesses of the waveguide, and optical alignment. As illustrated in Fig. 2 and using (3), the following three parameters can be readily extracted from the AWG-ring off-chip transmission spectrum:

$$T_r = \begin{cases} \eta\tau^2 \equiv T_{r,0} & \text{as } t_a/\tau \rightarrow 0 \\ \eta \left( \frac{\tau + t_a}{1 + \tau t_a} \right)^2 \equiv T_{r,\max} & \text{for } \Phi = \pi(1 + 2m) \\ \eta \left( \frac{\tau - t_a}{1 - \tau t_a} \right)^2 \equiv T_{r,\min} & \text{for } \Phi = 2\pi m, \end{cases} \quad (5)$$

where  $m \in \mathbb{Z}$ . By interpolating to the same wavelength the values of  $T_r$  found for each case in (5), three expressions can be computed for  $t_a$ :

$$\sqrt{\frac{T_{r,\max}}{T_{r,0}}} = \frac{\tau + t_a}{\tau(1 + \tau t_a)} \equiv R_a \Leftrightarrow t_a = \frac{\tau(R_a - 1)}{1 - \tau^2 R_a}, \quad (6)$$

$$\pm \sqrt{\frac{T_{r,\min}}{T_{r,0}}} = \frac{\tau - t_a}{\tau(1 - \tau t_a)} \equiv R_b \Leftrightarrow t_a = \frac{\tau(1 - R_b)}{1 - \tau^2 R_b}, \quad (7)$$

and

$$\pm \sqrt{\frac{T_{r,\max}}{T_{r,\min}}} = \frac{\tau + t_a}{\tau - t_a} \frac{1 - \tau t_a}{1 + \tau t_a} \equiv R_c \Leftrightarrow \tau(R_c - 1)t_a^2 + [(1 + R_c)(1 - \tau^2)] t_a + \tau(1 - R_c) = 0. \quad (8)$$

The parameters  $T_{r,0}$ ,  $T_{r,\max}$ , and  $T_{r,\min}$ , defined in (5), are proportional to  $\eta$ . In contrast, the AWG on-chip transmittance  $t_a$  is independent of  $\eta$ , as calculated from (6), (7), (8). However, other sources of uncertainty are introduced to these extracted values due to the interpolation. A rigorous analysis is discussed in Sect. 4.2.2. Notice from (7) and (8) that both  $R_b$  and  $R_c$  are negative when  $t_a > \tau$  and positive otherwise. The correct sign is found by first evaluating  $R_a$  from (6), since it is always positive, and then determining for which wavelengths  $t_a > \tau$ . The coefficient  $\tau$  should also be extracted independent of  $\eta$ . This is achieved in Sect. 4.2.2 by analyzing the transmittance of an unbalanced Mach-Zehnder interferometer (UMZI) with identical couplers to that of the AWG-ring [48].

Table 1. Design parameters for each AWG.

|                            |                     |                      |
|----------------------------|---------------------|----------------------|
| Number of channels         | $N_{\text{ch}}$     | 8                    |
| Number of AWs              | $N_{\text{AW}}$     | 117                  |
| Rowland radius             | $r$                 | 204.42 $\mu\text{m}$ |
| AW length increment        | $\Delta L$          | 15.55 $\mu\text{m}$  |
| i/o waveguide length       | $L_{\text{io}}$     | 1.60 mm              |
| AW width                   | $w_{\text{AW}}$     | 1.20 $\mu\text{m}$   |
| AW width at FPR            | $w_{\text{AW-FPR}}$ | 1.00 $\mu\text{m}$   |
| i/o waveguide width        | $w_{\text{io}}$     | 0.80 $\mu\text{m}$   |
| i/o waveguide width at FPR | $w_{\text{io-FPR}}$ | 1.20 $\mu\text{m}$   |
| AW pitch at FPR            | $d_{\text{AW-FPR}}$ | 1.25 $\mu\text{m}$   |
| i/o waveguide pitch at FPR | $d_{\text{io-FPR}}$ | 3.60 $\mu\text{m}$   |
| Footprint area             | $S$                 | 2.10 $\text{mm}^2$   |

### 3. Methods

#### 3.1. Coupling design

Three identical AWGs, AWG-rings, and UMZIs are fabricated on the same chip, along with two spiral waveguides. Fifteen straight waveguides are placed throughout the chip to study the variation in  $\eta$ . A cross-section scanning electron micrograph (SEM) of the bus waveguide is shown in Fig. 3(a). Although other reported Si AWGs use a thinner waveguide core [19], a 0.50- $\mu\text{m}$  thickness is used here for compatibility with the III/V-Si heterogeneous integration platform. This supports reduced propagation loss, coupling loss to optical fiber, and phase errors in the AWG [18]. Micrographs of an AWG and of an AWG-ring are shown in Fig. 3(b) and Fig. 3(c), respectively. The input and output facet design is schematized in Fig. 3(d). Notice that the Si waveguide at the facet is 6.00- $\mu\text{m}$  wide and tilted by  $7^\circ$  with respect to the normal to reduce internal reflections. The waveguide width is linearly tapered from 6.00  $\mu\text{m}$  to 0.95  $\mu\text{m}$  over a 200- $\mu\text{m}$  length to filter out the higher-order modes arising from the angled-facet reflection of the fundamental mode. It is then bent by  $7^\circ$  with a 200- $\mu\text{m}$  radius to align normal to the facet. The device in the center of Fig. 3(d) represents a straight waveguide, an AWG, a UMZI, or an AWG-ring.

#### 3.2. Device fabrication

As seen in Fig. 3(a), fabrication starts with a Si-on-insulator (SOI) wafer (100-mm in diameter) containing a 0.50- $\mu\text{m}$  thick Si layer on top of a 1.00- $\mu\text{m}$  thick buried  $\text{SiO}_2$  layer. Features are

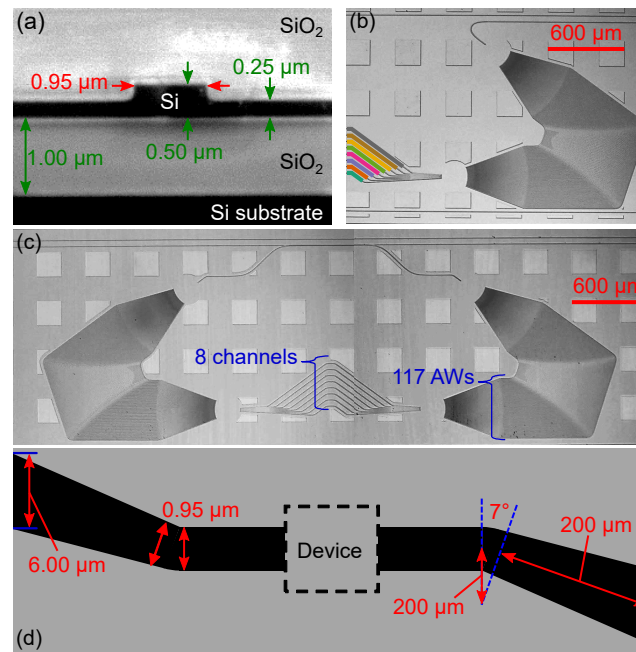


Fig. 3. (a) Cross-section SEM of the bus waveguide. Micrographs (b) of an AWG and (c) of an AWG-ring. (d) Top-view schematic of the facet design.

defined with deep-ultraviolet lithography and  $\text{SF}_6/\text{C}_4\text{F}_8/\text{Ar}$  reactive ion etching to remove  $0.25\ \mu\text{m}$  of Si. A 4:1 mixture of sulfuric acid and hydrogen peroxide held at  $80\ ^\circ\text{C}$  strips the photoresist. A  $1.00\text{-}\mu\text{m}$  thick  $\text{SiO}_2$  layer is then sputtered to form the top cladding before dicing the wafer and polishing the facets.

### 3.3. Experimental setup

Transmission spectra are measured by coupling light from a tunable laser (TL, Keysight 81680A) through each device, as depicted in Fig. 4. The TL is attached to a polarization-maintaining (PM) fiber (Thorlabs P5-1550PMAR) via an FC/APC connector. The other end of the PM fiber is FC/PC anti-reflective coated and connected to a collimating lens (CL, Thorlabs PAF-X-2-C). Light is then incident on a polarization beam splitter (PBS, Thorlabs CM1-PBS254) oriented to transmit on-chip transverse-electric polarization, which the focusing lens (FL, Thorlabs C230TM-C) directs onto the device waveguide facet. Output light is then collected with a single-mode lensed fiber (OZ Optics) attached to a v-groove fiber holder (FH, Thorlabs HFV002), and connected (FC/APC) to a power sensor (PS, Keysight 81634B). Input and output device coupling alignment is realized with 3-axis piezo-controlled flexure stages (Thorlabs MAX312). Waveguide loss characterization is accomplished by replacing the TL with an optical frequency domain reflectometry (OFDR) unit (LUNA OBR 4400) for these measurements [49].

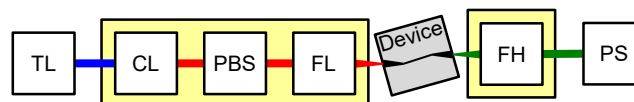


Fig. 4. Schematic of the experimental setup to measure transmission spectra. The optical beam drawn in blue is in a PM fiber, the red one in free-space, and the green one in a single-mode fiber. Yellow boxes represent 3-axis flexure stages.

## 4. Results and discussion

### 4.1. Waveguide transmission

The blue and the black curves in Fig. 5(a) respectively show one off-chip transmission spectrum  $T_w$  and the value  $\bar{T}_w$  averaged over all straight waveguide measurements ( $N_w = 43$ ). These values are obtained by normalizing the straight waveguide spectra to the transmission of the TL connected directly to the PS with the PM fiber. The standard deviation  $\sigma$  is then extracted, along with the coefficient of variation [50]:  $V_w \equiv \sigma/\bar{T}_w$ . This parameter, plotted in Fig. 5(b), does not explicitly depend on the transmittance. It represents variations between samples by normalizing the standard deviation ( $\sigma$ ) to the mean value ( $\bar{T}_w$ ). Therefore, it is suitable for describing the relative uncertainty on the coupling efficiency ( $\eta$ ).

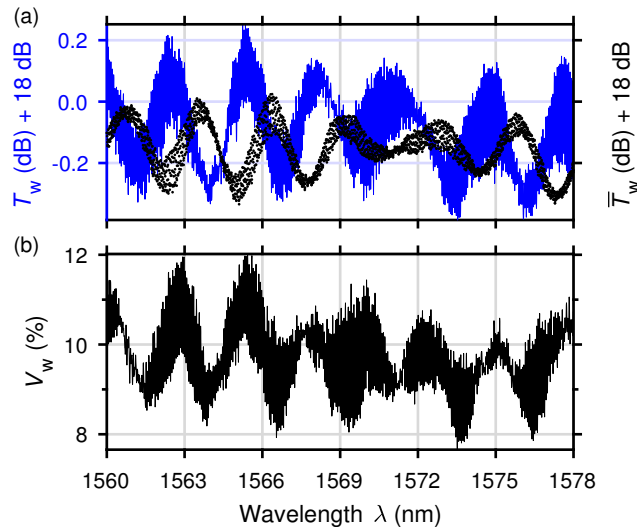


Fig. 5. (a, left axis) One off-chip transmission spectrum  $T_w$  measured for a straight waveguide and (a, right axis) transmission spectrum  $\bar{T}_w$  averaged over all straight waveguide measurements. (b) Spectrum of the coefficient of variation  $V_w$ .

Fluctuations in  $T_w$  between measurements either arise from variation in  $\eta$  or from on-chip scattering. To investigate this, the OFDR signal of a spiral waveguide covering  $5 \text{ mm}^2$  is acquired and plotted in Fig. 6. These data suggest that on-chip scattering is completely uniform. Consequently, the values of  $V_w$  obtained in Fig. 5(b) are only due to variation in  $\eta$  between measurements. A dual fit with logarithmic and constant dependencies is used to extract a loss coefficient  $\alpha = 70.9(2.0) \text{ dB/m}$ , where the number in parentheses is the standard uncertainty referred to the corresponding last digits of the quoted result. Although this value is comparable to similar Si waveguides [48], a fabrication process with reduced impurities and sidewall roughness is accessible and likely to improve it [51].

### 4.2. On-chip AWG transmission

On-chip transmission spectra  $t_a$  are extracted for each channel of an AWG using the waveguide normalization method [19]. Results are presented in Fig. 7(a) and discussed in Sect. 4.2.1. A more accurate extraction by the AWG-ring method of the same data is plotted in Fig. 7(b) and discussed in Sect. 4.2.2. The dynamic range of each AWG channel is usually characterized in terms of the loosely defined crosstalk (XT) [3]. A more rigorous and relevant figure-of-merit is

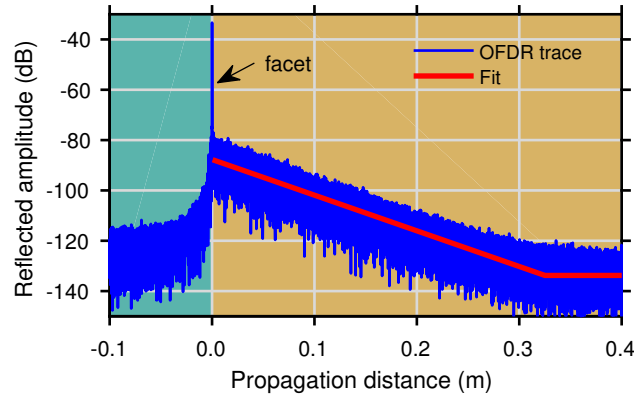


Fig. 6. OFDR signal (in blue) of a spiral waveguide with a dual fit (in red).

the 3-dB *cumulative crosstalk* (CXT). For channel  $x$ , it is defined as:

$$\text{CXT}_x \equiv \frac{\int_{3\text{dB},x} t_{a,x} d\lambda}{\int_{3\text{dB},x} \left( \sum_{y=1}^{N_{\text{ch}}} t_{a,y} - t_{a,x} \right) d\lambda}, \quad (9)$$

where the integrals span the 3-dB spectral bandwidth around the peak of each channel denoted by  $x$  or  $y$ . This parameter is indicated with disks in Fig. 7 for each AWG channel  $x = 1, 2, \dots, N_{\text{ch}}$ . Another convenient quantity is the mean 3-dB CXT per channel, defined as:

$$\overline{\text{XT}} \equiv \frac{1}{N_{\text{ch}} - 1} \sum_{x=1}^{N_{\text{ch}}} \text{CXT}_x. \quad (10)$$

The crosstalk scales with the number of channels, so  $\overline{\text{XT}}$  is suitable for comparing different AWG designs.

#### 4.2.1. Waveguide method

With the waveguide normalization method [19], on-chip transmission of an AWG is extracted as:

$$t_a = T_a / T_w, \quad (11)$$

where  $T_a$  is its off-chip transmission and  $T_w$  is the off-chip transmission of a nearby straight waveguide (see Fig. 5). The coefficient of variation  $V_w$  has a spectral average given by:

$$\langle V_w \rangle = \frac{1}{\lambda_f - \lambda_0} \int_{\lambda_0}^{\lambda_f} V_w d\lambda, \quad (12)$$

with  $\lambda_0 = 1560$  nm and  $\lambda_f = 1578$  nm. The uncertainty on  $t_a$  is then [50]:  $\Delta t_a|_{(11)} = \sqrt{2} \langle V_w \rangle$ . Values for  $\Delta t_a$ ,  $\overline{\text{XT}}$ , the minimum peak channel loss ( $L_{\text{min}}$ ), and the maximum peak channel loss ( $L_{\text{max}}$ ) are listed in Table 2. While these values reveal good performance of this Si AWG, the relative uncertainties are large.

#### 4.2.2. AWG-ring method

With the AWG-ring method,  $t_a$  is extracted from Eq. (5). Its uncertainty can be evaluated once those on  $T_{r,0}$ ,  $T_{r,\text{max}}$ ,  $T_{r,\text{min}}$ , and  $\tau$  are found. The transmission  $T_{w,l}$  of a straight waveguide denoted

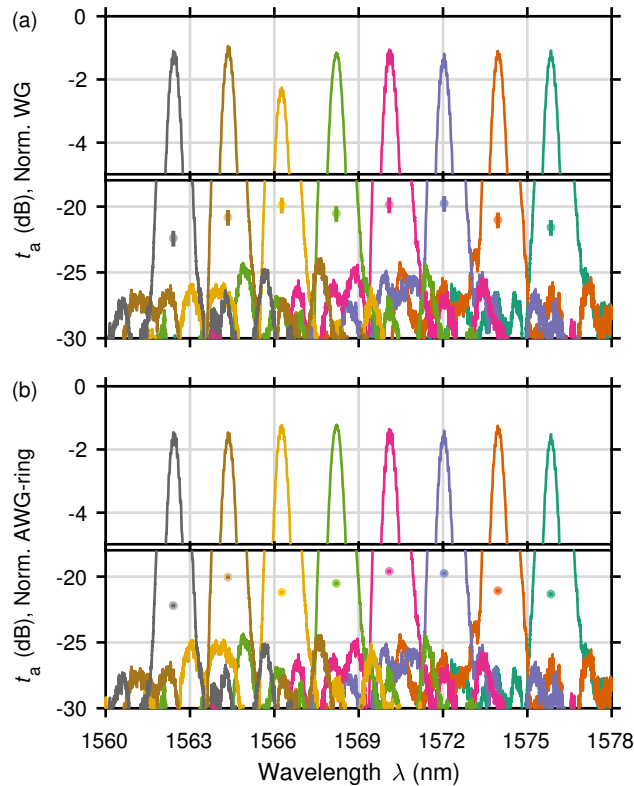


Fig. 7. On-chip transmission spectra  $t_a$  extracted for each channel of a single AWG. Normalization is performed (a) with the waveguide method and (b) with the AWG-ring method. Disks indicate the 3-dB CXT for each channel with their respective uncertainty.

$l$  has a coefficient of variation  $V_{w,l}$ , calculated within a spectral range  $\delta\lambda$ . The uncertainty on each  $T_r$  is given by:

$$\Delta T_r = \frac{1}{N_w N_s} \sum_{l=1}^{N_w} \sum_{m=1}^{N_s} V_{w,l}(\lambda_{m-1}; \lambda_m), \quad (13)$$

where  $N_s \equiv (\lambda_f - \lambda_0)/\delta\lambda$  and  $\lambda_m = \lambda_0 + m\delta\lambda$ . For (6) and (7),  $\delta\lambda$  is 3/2 the AWG channel spacing, and for (8), it is 3/2 the AWG-ring free spectral range (FSR). These values correspond to the spectral range that is necessary to interpolate each expression in Eq. (5). When evaluating (13) for each  $T_r$  appearing in (6) and (7), the spectral range is  $\delta\lambda = 3.0$  nm and  $\Delta T_r \cong 2.95$  %. For (8),  $\delta\lambda = 0.1$  nm and  $\Delta T_r \cong 2.93$  %.

The coupling parameter  $\tau^2$  is extracted from the UMZI transmission spectra [48] and plotted in Fig. 8 along with its uncertainty  $\Delta\tau^2$ . This includes uncertainty due to  $\eta$  and additional variation arising from fabrication. The parameter  $\Delta\tau^2$  has a spectral average  $\langle\Delta\tau^2\rangle \cong 2.92$  %.

Near critical coupling, where  $\tau = t_a^2$  [46], additional uncertainty is introduced when interpolating the  $T_{r,\min}$  values, which should vanish. Due to the finite FSR of the AWG-ring, interpolated values for  $T_{r,\min}$  are not accurate as  $t_a^2$  approaches  $\tau$ . The value of  $\tau$  should thus be smaller than  $t_a$  for a  $\sim 2$ -dB bandwidth within the peak transmission of each channel to provide sufficient extracted data of  $t_a$ . However, decreasing  $\tau$  increases  $T_{r,\min}$  near the peak channel transmittance and subsequently increases the absolute uncertainty on  $t_a$ . From these considerations, the following is chosen:  $\tau = \sqrt{0.15} \cong -4.12$  dB. This allows to resolve a  $\sim 2$ -dB bandwidth for channels with  $-2$ -dB peak transmittance.

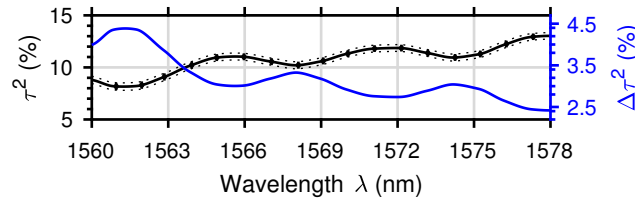


Fig. 8. Coupling parameter  $\tau^2$  (left axis) extracted from the UMZI transmission spectra. The uncertainty  $\Delta\tau^2$  is plotted on the left axis in dotted black lines and on the right axis in blue.

The AWG on-chip transmittance  $t_a$  is extracted in Fig. 9, using the model expressed in (3). Substituting the values of  $\Delta\tau^2$ ,  $\Delta T_{r,0}$ ,  $\Delta T_{r,\max}$ , and  $\Delta T_{r,\min}$  in the uncertainty propagation equation [50] obtained from (6), (7), and (8) allows to extract  $\Delta t_a$  for each case of the AWG-ring method. These values are listed in Table 2.

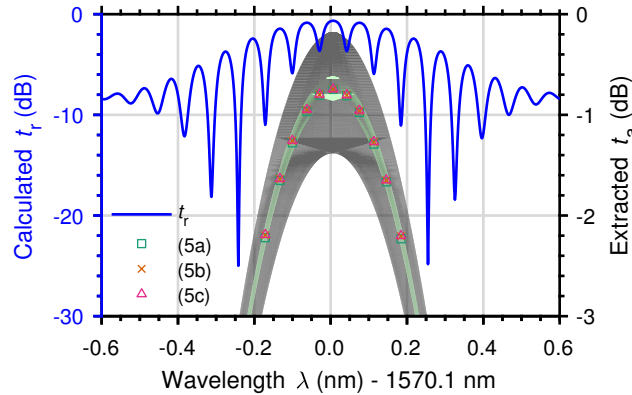


Fig. 9. Calculated AWG-ring on-chip transmission spectrum (left axis) and (right axis) extracted AWG on-chip transmittance. The grey and the light-green areas respectively delimit the uncertainties from the conventional and the present methods.

Table 2. Summary of on-chip AWG transmission  $t_a$ .

| Method | $\Delta t_a$ (%) | $\overline{XT}$ (dB) | $L_{\min}$ (dB) | $L_{\max}$ (dB) |
|--------|------------------|----------------------|-----------------|-----------------|
| (6)    | 6.65             | -29.05(28)           | 0.98(29)        | 1.72(29)        |
| (7)    | 2.74             | -29.08(12)           | 1.18(12)        | 1.60(12)        |
| (8)    | 3.07             | -29.09(13)           | 1.22(13)        | 1.52(13)        |
| (11)   | 13.74            | -29.09(56)           | 0.95(60)        | 2.26(60)        |

On-chip AWG transmittance is extracted by applying (6), (7), and (8) to the measured AWG-ring off-chip transmission spectrum. This is illustrated in Fig. 10, where the transmittance near the peak of channel #5 is plotted. The AWG transmittance extracted using (6), (7), and (8) have overlapping uncertainty ranges, as expected, and (7) is the most accurate. Outside a 1-dB bandwidth from the resonance, the uncertainties increase drastically as critical coupling occurs and  $t_a^2$  approaches  $\tau$ . However, these data are not needed for normalization.

The entire transmission spectrum of an AWG-ring is now used to extract  $t_a$  for each AWG channel. From AWG-ring data shown in Fig. 11, the transmission within  $\sim 1$  dB of the peak for each channel of  $t_a$  are extracted. Normalization is performed in Fig. 7(b) on transmission data of a

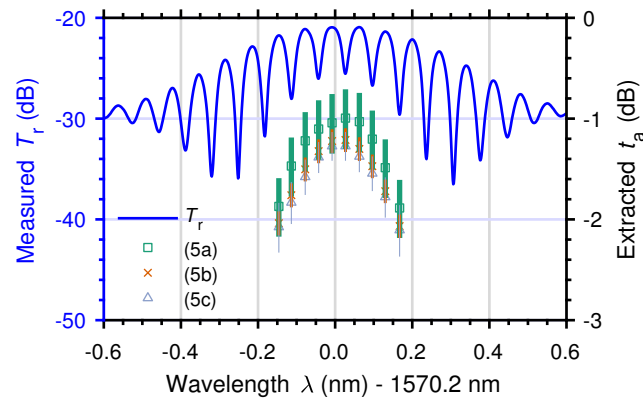


Fig. 10. (Left axis) Measured AWG-ring off-chip transmission spectrum  $T_r$  and (right axis) AWG on-chip transmission spectrum  $t_a$  extracted using the 3 expressions introduced in Eq. (5).

single AWG with the peak channel transmission obtained from (7), shown in Fig. 11. Results are listed in Table 2. The peak channel wavelength is measured in three AWGs, revealing a standard deviation of  $\sim 138$  pm. Therefore, the loss may be overestimated with the AWG-ring method due to misalignment of the channels, *i.e.* the values in Table 2 may be at most 0.16 dB higher than the actual loss. In addition, the value for XT is, to our knowledge, the lowest reported for a Si AWG [19]. This crosstalk level is likely limited by the thickness variation of the Si core [18, 52]. Contributions to  $L_{\min}$  are due to reflections at the FPR-AW transition ( $\sim 0.55$  dB), the grating side-order excitations ( $\sim 0.47$  dB), the limited grating aperture ( $\sim 0.09$  dB), and scattering loss ( $\sim 0.08$  dB).

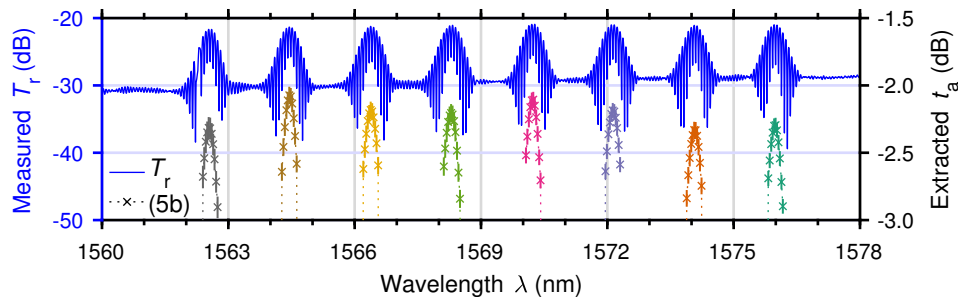


Fig. 11. (Left axis) Measured AWG-ring off-chip transmission spectrum  $T_r$  and (right axis) on-chip transmission spectra  $t_a$  extracted for each AWG channel using (7).

## 5. Conclusion

A low-loss Si AWG operating in the near-infrared is demonstrated with accurately reported peak channel transmittance and crosstalk level. An AWG-ring is proposed and used to characterize the peak transmittance of each AWG channel. Compared to the uncertainty on  $t_a$  obtained with the waveguide normalization method, an improvement by 80.1 % is demonstrated with (7). On-chip transmission is demonstrated in the range of 69–76 % with crosstalk per channel of  $-29$  dB. While this work reports on a low-loss AWG, more advanced design [16] and improved fabrication [51] are expected to further reduce the loss and the crosstalk. The AWG-ring method proposed

here should be used to measure incremental progress on AWG design, thus yielding significant improvements in total transmission efficiency for AWGs with large numbers of channels.

### **Funding**

Air Force Research Laboratory (AFRL) (FA8650-17-C-5402); Office of Naval Research (ONR) (N00014-13-C-0147); N. V. acknowledges support from the Swiss National Science Foundation.

### **Acknowledgments**

The authors thank Michael L. Davenport for fabrication advice, Alexander Spott for helpful feedback, and the UCSB Nanofabrication Facility for technical support.

### **Disclosures**

The authors declare that there are no conflicts of interest related to this article.